

# Nanogranular Origins of the Strength of Bone

Kuangshin Tai,<sup>†</sup> Franz-Josef Ulm,<sup>‡</sup> and Christine Ortiz<sup>\*†</sup>

*Department of Materials Science and Engineering and Department of Civil Engineering, Massachusetts Institute of Technology, 77 Massachusetts Avenue, Cambridge, Massachusetts 02139*

*Received August 10, 2006; Revised Manuscript Received September 13, 2006*

## ABSTRACT

Here, we investigate the ultrastructural origins of the strength of bone, which is critical for proper physiological function. A combination of dual nanoindentation, three-dimensional elastic-plastic finite element analysis using a Mohr-Coulomb cohesive-frictional strength criterion, and angle of repose measurements was employed. Our results suggest that nanogranular friction between mineral particles is responsible for increased yield resistance in compression relative to tension and that cohesion originates from within the organic matrix itself, rather than organic–mineral bonding.

The ultrastructural origins of the plasticity of bone and its complex relationship to damage accumulation and fracture risk are poorly understood. Recent studies<sup>1–3</sup> have primarily probed tensile modes of deformation, which are relevant, for example, to avulsion fractures at tendinous and ligamentous insertions and bending fractures in the diaphyseal regions of long bones.<sup>4</sup> In this study, we focus on the nanoscale compressive strength of bone, which is a significant physiological loading condition<sup>5</sup> and a key requirement *in vivo*. While day-to-day deformation of bone generally takes place in the linear elastic regime,<sup>6</sup> excessive injurious loads, fatigue, and degradation of biomechanical properties due to age or disease can lead to microdamage<sup>7</sup> and fracture<sup>8</sup> *in vivo* at compressive locations such as metaphyseal areas, vertebral bodies, and the calcaneus.<sup>4</sup> Hence, a fundamental mechanistic understanding of how the structural design of bone is able to achieve optimal resistance to compressive yield is critically important for predicting tissue-level fracture, simulating remodeling processes, and developing clinical approaches to treat biomechanical degradation.

It is known that cortical bone exhibits a macroscopic yield strength in compression that is greater ( $\sim 2\times$ ) than in tension or torsion,<sup>9</sup> which is indicative of pressure sensitive plasticity. The strength of bone must begin at the ultrastructural level. At this length scale, plate-like carbonated apatite mineralites exist ( $\sim 10$  s of nm in length and width, 3–5 nm in thickness<sup>10</sup>) that permeate in and around type I collagen

fibrils in an overlapping manner.<sup>1</sup> In this paper, we explore the possibility of nanogranular friction from mineral–mineral interparticle interactions as a contributing source of the compressive yield strength of bone. This hypothesis is based on a number of experimental observations. First, the inorganic component is known to be a critical determinant of the macroscopic compressive mechanical properties of bone; the yield stress,<sup>11</sup> maximal stress,<sup>12</sup> and failure strength<sup>13</sup> are all known to increase with increasing mineral content. Second, the fact that mineral content of human bone is typically above the percolation threshold of 50% packing density (corresponding to  $\sim 43\%$  mineral content).<sup>14,15</sup> Last, previously reported data of the direct visualization of the ultrastructural plasticity of bone via nanoindentation combined with high resolution atomic force microscopy (AFM) imaging of residual impressions show the nanogranular structure of contacting mineralites flattened, but still visible, within the plastically deformed indented region (Figure 1).<sup>16</sup> The appearance of the undeformed mineralites outside of the indent region compared to within suggest mineral displacement and the possibility of interparticle frictional interactions. These data are consistent with recent scanning electron microscopy images of collagen fibrils bridging a crack within a compressed trabeculae.<sup>17</sup> Given that many mineralized fibrils are in direct contact with each other, deformation away from their unstressed configurations likely involve mineral–mineral displacement. Hence, we hypothesize that the ultrastructure of bone is a cohesive-frictional material,<sup>18</sup> following a Mohr-Coulomb pressure dependent strength criterion<sup>19</sup> (i.e., which arises from the pressure dependence of the density of interparticle contacts).

\* To whom correspondence should be addressed. Phone: 617-452-3084. Fax: 617-258-6936. E-mail: cortiz@mit.edu.

<sup>†</sup> Department of Materials Science and Engineering.

<sup>‡</sup> Department of Civil Engineering.

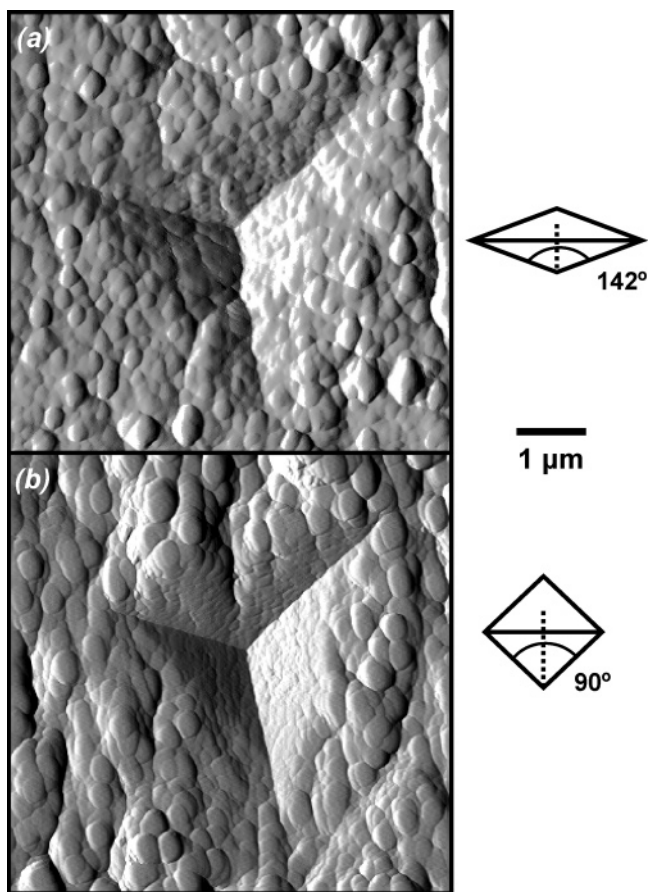


**Figure 1.** Tapping mode atomic force microscopy amplitude images (*Quesant*) of a residual nanoindentation impression in adult bovine cortical bone (~65 wt % measured through back-scattered electron imaging, which probes a depth of ~1  $\mu\text{m}$ ) immediately after loading to 7000  $\mu\text{N}$  followed by unloading (*Hysitron* Triboindenter, loading/unloading rate of 50  $\mu\text{N}/\text{second}$ ) using (a) Berkovich (~850 nm depth) and (b) Cube Corner (~1.5  $\mu\text{m}$  depth) geometry. Experiments were conducted with the loading direction perpendicular to the long bone axis in ambient conditions. Details of the sample preparation and characterization and experimental protocols were reported previously.<sup>16</sup> The undeformed regions away from the residual indent area are composed of nanogranular topographical features in contact with each other which have a heterogeneous shape and size distribution (maximum lateral dimension =  $51.0 \pm 30.7$  nm) which is consistent with the known dimensions of mineral particles, as measured by scanning electron microscopy,<sup>41</sup> transmission electron microscopy,<sup>42</sup> and small-angle X-ray scattering.<sup>43</sup>

To explore this hypothesis, the nanoindentation of cortical bone was predicted using an elastic-plastic three-dimensional finite element analysis (FEA) model for two independent triaxial stress states<sup>20</sup> achieved with two different indenter geometries, Berkovich (included angle  $142.3^\circ$ , half angle  $65.3^\circ$ ) and Cube Corner (included angle  $90^\circ$ , half angle  $54.6^\circ$ ), which incorporated the Mohr-Coulomb pressure dependent strength criterion. In this case, the strength domain in the principal stress space,  $\sigma_I \geq \sigma_{II} \geq \sigma_{III}$ , is defined by

$$f(\sigma_{ij}) = \sigma_I(1 + \sin \varphi) - \sigma_{III}(1 - \sin \varphi) - 2c \cos \varphi \leq 0 \quad (1)$$

where  $c$  is the interparticle cohesion, which is the finite value

of cohesive shear strength required to cause sliding when the normal stress is zero, and  $\varphi$  is the internal friction angle, which provides the failure envelope given by the relationship of the linear slope between shear and normal stress. This internal friction approaches the “dry” (zero cohesion) angle of repose, which is measured when a bulk quantity of particles is poured onto a horizontal surface and is defined as the angle formed by the inclined edge of the pile and the horizontal plane. The FEA model utilized large deformation theory and incorporated a rigid indenter with frictionless contacts between the tip and sample. A modulus of 18 GPa was fixed in the simulations and approximated from the unloading slope of the nanoindentation data using an isotropic, elastic continuum mechanical half-space formulation.<sup>21</sup> A Poisson’s ratio of 0.3 was also fixed.<sup>22</sup> Two material properties were reduced from the experimental data:  $c$  and  $\varphi$ , which were free fitting parameters. The difference between the experimental indentation response and the theoretical predictions were minimized by the quadratic error for values that best fit both indenter geometries.

The predictions of the theoretical fits were compared to nanoindentation force versus indentation depth data taken on loading of adult bovine cortical bone perpendicular to the long bone axis for both the Berkovich and Cube Corner geometries (Figure 2). The sample preparation, characterization, and experimental protocols have been reported previously.<sup>16</sup> The best fit  $\varphi$  and  $c$  values for both indenter geometries were found to be  $15^\circ$  and 100 MPa, respectively ( $R^2 = 0.99$ ). The indentation simulations on loading exhibited a small elastic region (indentation depths  $< \sim 10$  nm) followed by yield (as assessed by monitoring the plastic equivalent strain of each element) due to local stress concentrations at the tip apex. The friction angle that best fits both indenter geometries translates into a uniaxial compressive strength-to-tensile-strength ratio ( $Y_c/Y_t = (1 + \sin \varphi)/(1 - \sin \varphi)$ ) of 1.7, which is remarkably close to the known macroscopic ratio  $\sim 2$ .<sup>9</sup> Theoretical fits were also carried out on nanoindentation data taken on fully demineralized bone (treated for 5 days in 0.5 M ethylenediaminetetraacetic acid). The modulus was fixed to that reduced from the unloading slope ( $\sim 2.3$  GPa) and Poisson’s ratio was set to 0.3 as previously, yielding best fit  $\varphi$  and  $c$  values for both indenter geometries of  $5^\circ$  and 100 MPa, respectively (Figure 3) translating to a compressive strength-to-tensile-strength ratio of 1.2. Figure 4 compares all four experimental nanoindentation datasets on a single plot and shows an increased force for a given depth (i.e., resistance to yield) for the intact compared to demineralized bone.

We note in Figure 1 the absence of pileup and rather the presence of sink-in which is explained as follows. The ultrastructure of bone has been suggested to possess nanoscale porosity ( $\sim 20$  nm in size)<sup>23</sup> which is a characteristic of a nanogranular material. Hence, when bone is compressed during nanoindentation, there is most likely a plastic contracting behavior until the material reaches a state (called the critical state, a concept introduced for granular soils from which all Cam-Clay models derive<sup>24</sup>) at which it behaves like a cohesive-frictional material in the Mohr-Coulomb

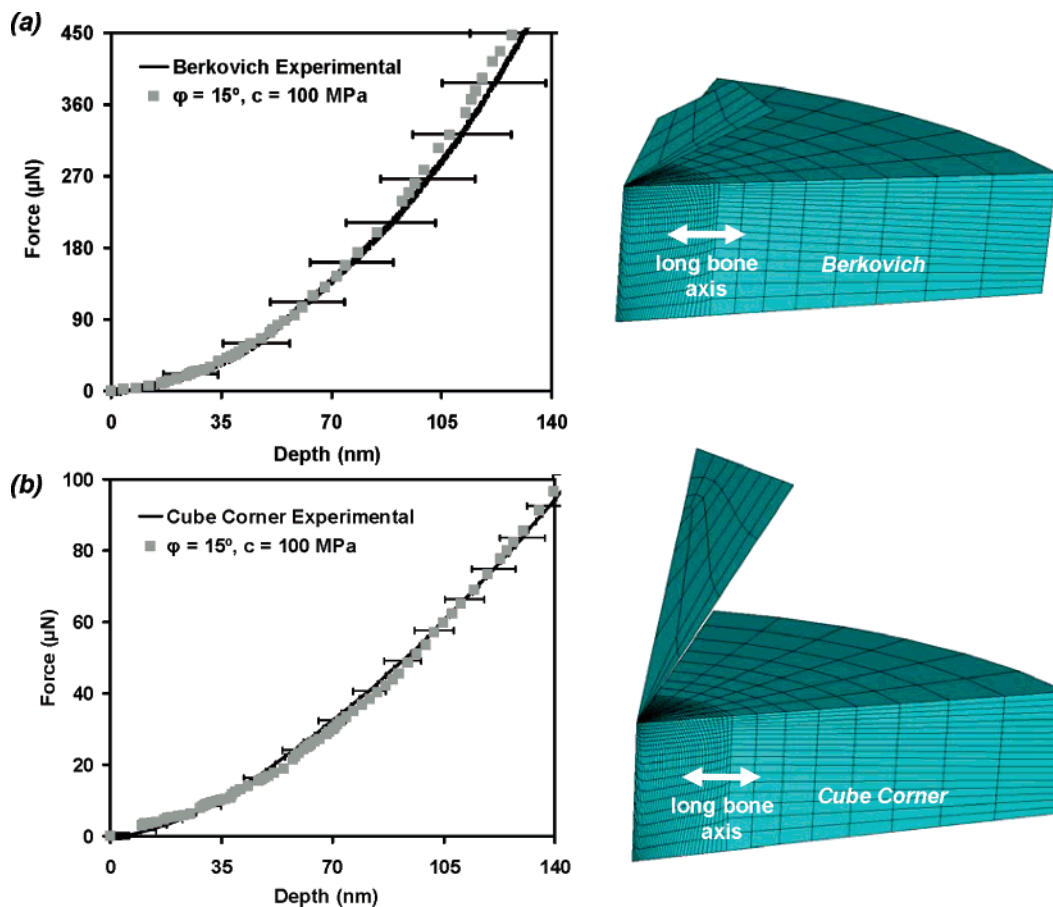


**Figure 2.** Comparison of the predictions of a three-dimensional elastic-perfectly plastic finite element analyses (FEA) model (ABAQUS) incorporating a Mohr–Coulomb cohesive-frictional yield strength criterion to averaged nanoindentation data on loading of intact adult bovine cortical bone perpendicular to the long bone axis in ambient conditions (*Hysitron* Triboindenter, loading rate  $\sim 50 \mu\text{N/s}$ ) using; (a) Berkovich and (b) Cube Corner probe tips. The sample preparation, characterization, and experimental protocols were reported previously.<sup>16</sup> The two fitting parameters used were the internal friction angle ( $\varphi$ ) and cohesion ( $c$ ). The best-fit parameters ( $R^2 = 0.99$ ) produced the same value for the two different indenter geometries. (a) Berkovich and (b) Cube Corner FEA meshes are also shown. Eight-node linear elastic brick hybrid elements (C3D8H) were used. To reduce computational cost and due to symmetry, 1/6 of the tip and the surface were modeled and the corresponding boundary conditions were applied to ensure the symmetry; that is, the nodes on the sidewalls were fixed in the direction normal to the sidewall surface (the nodal displacement in this direction is set to be zero). The probe tip end radius and truncate height were approximated from control experiments on a fused quartz sample. Each averaged force versus depth curve represents 80 individual nanoindentation experiments; horizontal bars are one standard deviation.

sense (i.e., the state which we model with FEA). In return, the plastic contracting behavior can explain why we observe sink-in rather than pile-up. This is observed in the AFM images (Figure 1): rather than being squeezed out, the particles in the imprint area are more highly compacted than far away. Refined models, currently in development, aim at taking this contracting behavior into account, by considering a critical-state Cam–Clay type plasticity model for bone nanoindentation. This refined model, which considers nano-scale porosity, is expected to shed light on the observable contracting behavior in nanoindentation, whereas it is not expected to change the overall result that bone’s ultrastructure is a cohesive-frictional material.

In order to further investigate the nanogranular friction in bone, angle of repose experiments were performed on ground and ultrasonicated powders of deorganified adult bovine cortical bone mineral (Figure 5) in a sealed chamber in ambient ( $\varphi_{\text{ambient}}$ ) and vacuum environments ( $\varphi_{\text{vacuum}}$ ). The smallest particle size distribution obtained was  $914 \pm 44$

nm (as measured by dynamic light scattering) and the corresponding angles of repose were found to be  $\varphi_{\text{ambient}} = 32.8 \pm 3.1^\circ$  and  $\varphi_{\text{vacuum}} = 18.2 \pm 2.5^\circ$  (number of measurements,  $n = 4$ ). Since  $\varphi_{\text{vacuum}} < \varphi_{\text{ambient}}$ , this suggests that the vacuum was effective in minimizing interparticle cohesion likely due to hydration layers.  $\varphi_{\text{vacuum}}$  was found to be statistically independent ( $p < 0.05$ ) of particle size up to  $25 \mu\text{m}$ . It was observed that the internal friction angle  $\varphi$  obtained from fitting nanoindentation data to the Mohr–Coulomb formulation in intact bone ( $\sim 15^\circ$ ) was slightly lower than the measured angle of repose in vacuum  $\varphi_{\text{vacuum}}$  ( $\sim 18.2^\circ$ ) for the deorganified bone. Hence, rather than introducing additional friction due to macromolecular shear (as might be expected since  $\varphi = 5^\circ$  for the demineralized bone), the interfacial organic has a slight lubricating effect, which is consistent with nanomechanical studies which show that certain interfacial organics, in particular polyelectrolyte macromolecules, can enhance lubrication.<sup>25</sup> This may be a tradeoff effect, in order to counteract the reduction of tensile

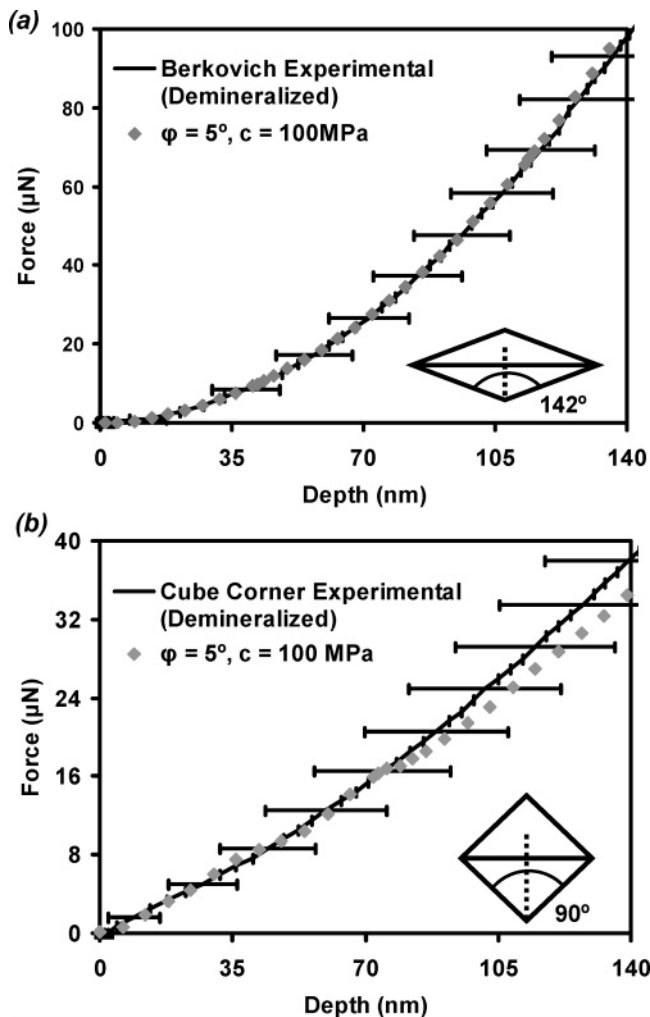


**Figure 3.** Adult bovine cortical bone was demineralized using 0.5 M ethylenediaminetetraacetic acid treatment for 5 days. Lack of mineral was verified through X-ray photoelectron spectroscopy (no evidence of Ca or P), heat treatment (400 °C to show complete loss of material), and energy dispersive X-ray analysis (no Ca, P). A three-dimensional elastic-perfectly plastic finite element analyses (FEA) model incorporating the Mohr-Coulomb cohesive-frictional strength criterion (described in Figure 2 caption) was fit to the averaged experimental nanoindentation force versus depth curve for demineralized bone tested perpendicular to the long bone axis in ambient conditions for (a) Berkovich and (b) Cube Corner probe tips ( $R^2 = 0.99$ ). Each averaged force versus depth curve represents 80 individual nanoindentation experiments; horizontal bars are one standard deviation.

capacity compared to the cohesive shear strength (primarily carried by the organic component) due to frictional interactions.

It is interesting to note that  $c$  (intact bone)  $\approx c$  (demineralized bone) which may well suggest that cohesion values quantified by nanoindentation are attributable to the organic itself, rather than to interfacial mineral-organic bonding.<sup>26</sup> Indeed, cohesion may arise from collagen crosslinking (which includes intermolecular pyridinoline and pyrrole linkages arising from linkages between lysine and hydroxylysine aldehyde residues<sup>27,28</sup>) or noncovalent “sacrificial” bonding in noncollagenous proteins (e.g., proteoglycans, osteopontin, and bone sialoprotein<sup>29,30</sup>).

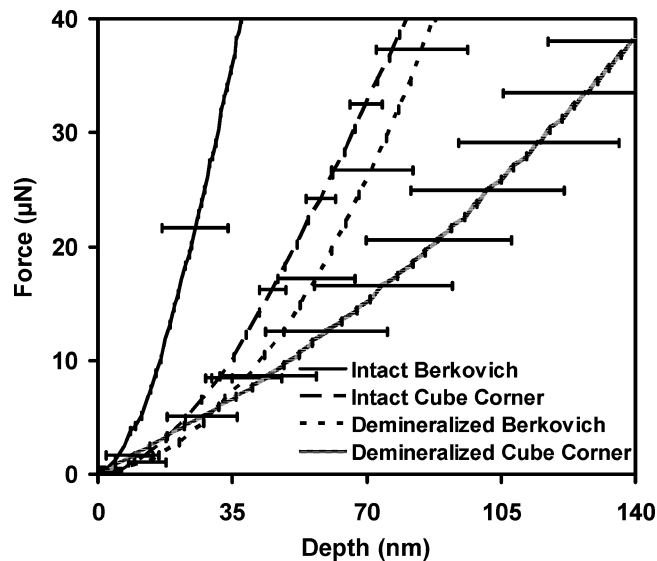


**Figure 4.** Plot comparing experimental nanoindentation data on loading in ambient conditions perpendicular to the long bone axis comparing intact (data from Figure 2) and demineralized (data from Figure 3) bone indented with both Berkovich and Cube Corner probe tips. Each averaged force versus depth curve represents 80 individual nanoindentation experiments; horizontal bars are one standard deviation.

The fact that  $\varphi$  (intact bone)  $\gg \varphi$  (demineralized bone) (Figures 2 and 3) and  $\varphi$  (intact bone)  $\approx \varphi_{\text{vacuum}}$  (deorganized bone) (Figures 2 and 5) suggests that the ultrastructural origins of the friction angle arise primarily from mineral interparticle interactions and that organic frictional contribution (e.g., internal friction arising from, for example, molecular rotations, stick–slip sliding, and/or barrier–hop fluctuations<sup>31</sup>) is minimal. Potential interparticle frictional mechanisms cited in the literature that may be relevant include mechanical interlocking and deformation of surface nanoasperities, which has been observed directly by scanning electron microscopy for adjacent aragonite-based nacre tablets (from the inner layer of a gastropod mollusk).<sup>32</sup> In this paper,<sup>32</sup> it was postulated that inter-tablet shear resistance was enhanced as nanoasperities were required to “climb” over one another in order for intertablet sliding. Another potential mechanism at even smaller length scales has been studied by atomistic molecular dynamics modeling and involves mechanical locking due to surface roughness between atoms, as well as dynamic friction characterized by translational kinetic energy that dissipates during sliding into internal energy motions.<sup>33</sup> Stick–slip and smooth sliding between atoms and the transition between the two at atomic length scales could be relevant to bone mineral interactions as well.<sup>34</sup>

The addition of mineral and corresponding frictional interactions results in an increase in the resistance to plasticity (strength or elasticity domain) in compression at these small lengths (Figure 4), which is the dominating physiological stress state in bone, and correlates with the correct trend macroscopically.<sup>11</sup> Our interpretation is consistent with the known structure–function relationships of other mineralized tissues; for example, human tendon has no mineral volume and is loaded predominantly in tension,<sup>35</sup> whereas ear or whale bones have a considerable amount of mineral ( $\sim 90$

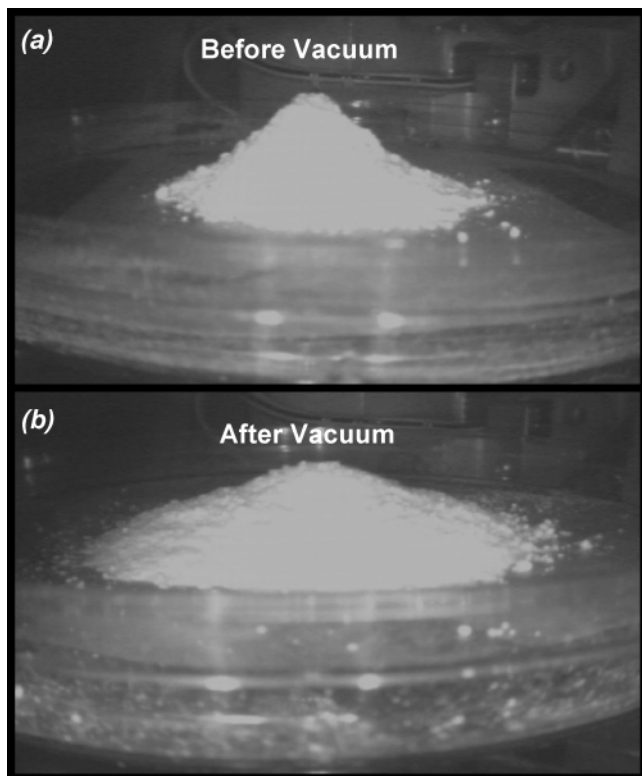


**Figure 5.** Angle of repose experiments performed in ambient environmental conditions and in vacuum. The deorganified bone (400 °C heat treatment where no weight change after 5 days was recorded) powder is shown (a) before vacuum, ambient conditions and (b) after vacuum. Angles measured from deorganified bone were compared to one another and found to be  $\sim 33^\circ$  in the ambient state and  $\sim 18^\circ$  in vacuum. The particle size was varied ( $\sim 1\text{--}25\ \mu\text{m}$ ) and controlled by the degree of sonication (Branson, Sonifier 450) and measured by a Brookhaven 90Plus Particle Size Analyzer. The angle of repose did not change significantly for the range of particle sizes measured.

wt %) and are primarily loaded in compression.<sup>14</sup> Human (as well as bovine) bone ( $\sim 60$  wt % mineral) seems to be an intermediate compromise, providing strength in compression for physiological loading plus some degree of protection for accidental shear/torsion/bending loading. Mineralization has also been shown to vary with anatomical site,<sup>36</sup> leading to correlated intersite variation in compressive stiffness<sup>37</sup> (reflective of mineral content) and yield strength.<sup>38</sup>

The macroscopic experimental value of the uniaxial compressive yield strength of these adult bovine cortical bone samples was measured perpendicular to the long bone axis as  $\sigma_y \sim 178 \pm 47$  MPa (Zwick allround-line mechanical tester, 0.01 mm/s load rate), which is 30% less than that calculated from the Mohr–Coulomb friction angle and cohesion reduced from nanoindentation data ( $\sim 260$  MPa). This comparison suggests that larger length scale structures serve to weaken, rather than strengthen bone, possibility due to heterogeneity, porosity, or other defects present.

A number of nanoscale deformation mechanisms have been proposed in the literature, based on various types of experimental data, including void and crack formation,<sup>39</sup> extension of bridging noncollagenous proteins with sacrificial bonds during collagen fibril separation,<sup>1</sup> and mineralized

collagen fibril-matrix shear.<sup>2</sup> Several of these behaviors are expected to be pressure dependent (i.e., consistent with macroscopic yield). These mechanisms were all observed primarily in tensile modes of deformation. No distinct microcracking was observed in the direct imaging of the compressive deformation (Figure 1), but it should be noted that very small loads and lengths scale are being probed, and hence, our results do not preclude this mechanism from taking place at larger deformations. No jumps or discontinuities were observed in the individual force versus depth curves as well (data not shown) suggesting the absence of underlying microcracking<sup>40</sup> and a uniform continuum response. The mineralized collagen fibril-matrix shear mechanism in tension could in fact activate the mechanism proposed here, mineralite interparticle friction, as well as rupture of sacrificial bonds in the organic.<sup>1</sup> Our results suggest, however, that the former is more dominant for this particular compressive experimental geometry studied and is an important factor in the pressure-dependent yield strength of bone.

**Acknowledgment.** The MIT Department of Materials Science and Engineering Nanomechanical Testing Facility, The Whitaker Foundation and the U.S. Army through the MIT Institute for Soldier Nanotechnologies (Contract No. DAAD-19-02-D0002) for funding. [The content does not necessarily reflect the position of the government and no official endorsement should be inferred.]

## References

- (1) Fantner, G. E.; Hassenkam, T.; Kindt, J. H.; Weaver, G.; Birkedal, H.; Pechenik, L.; Cutroni, J. A.; Cidade, A.; Stucky, G.; Morse, D. E.; Hansma, H. G. Sacrificial bonds and hidden length dissipate energy as mineralized fibrils separate during bone fracture. *Nat. Mater.* **2005**, *4*, 612–616.
- (2) Gupta, H. S.; Wagermaier, W.; Zickler, G. A.; Raz-Ben Aroush, D.; Funari, S. S.; Roschger, P.; Wagner, H. D.; Fratzl, P. Nanoscale deformation mechanisms in bone. *Nano Lett.* **2005**, *5* (10), 2108–2111.
- (3) Nalla, R. K.; Kinney, J. H.; Ritchie, R. O. Mechanistic fracture criteria for the failure of human cortical bone. *Nat. Mater.* **2003**, *2*, 164–168.
- (4) Cochran, G. V. B. *A primer of orthopaedic biomechanics*; Churchill Livingstone: New York, 1982.
- (5) Nordin, M.; Frankel, V. Biomechanics of Bone. In *Basic Biomechanics of the Musculoskeletal System*; Lea & Febiger: Philadelphia, 1989; Number of 3–29.
- (6) Biewener, A. A. Safety factors in bone strength. *Calcif. Tiss. Int.* **1993**, *53 Suppl 1*, S68–74.
- (7) Vashishth, D.; Koontz, J.; Qiu, S. J.; Lundin-Cannon, D.; Yeni, Y. N.; Schaffler, M. B.; Fyhrie, D. P. In vivo diffuse damage in human vertebral trabecular bone. *Bone* **2000**, *26* (2), 147–152.
- (8) Fine, K. M.; Vegso, J. J.; Sennett, B.; Torg, J. S. Prevention of cervical spine injuries in football: A model for other sports. *Phys. Sportsmed.* **1991**, *19*, 54–62.
- (9) Yeni, Y. N.; Dong, X. N.; Fyhrie, D. P.; Les, C. M. The dependence between the strength and stiffness of cancellous and cortical bone tissue for tension and compression: extension of a unifying principle. *Biomed. Mater. Eng.* **2004**, *14* (3), 303–310.
- (10) Weiner, S.; Wagner, H. D. The material bone: Structure-mechanical function relations. *Ann. Rev. Mater. Sci.* **1998**, *28*, 271–298.
- (11) Wachter, N. J.; Krischak, G. D.; Mentzel, M.; Sarkar, M. R.; Ebinger, T.; Kinzl, L.; Claes, L.; Augat, P. Correlation of bone mineral density with strength and microstructural parameters of cortical bone in vitro. *Bone* **2002**, *31* (1), 90–95.
- (12) Louis, O.; Boulpaep, F.; Willnecker, J.; Van den Winkel, P.; Osteaux, M. Cortical mineral content of the radius assessed by peripheral QCT predicts compressive strength on biomechanical testing. *Bone* **1995**, *16* (3), 375–379.

- (13) Lotz, J. C.; Gerhart, T. N.; Hayes, W. C. Mechanical properties of trabecular bone from the proximal femur: a quantitative CT study. *J. Comput. Assist. Tomogr.* **1990**, *14* (1), 107–114.
- (14) Hellmich, C.; Ulm, F. J. Average hydroxyapatite concentration is uniform in the extracollagenous ultrastructure of mineralized tissues: evidence at the 1–10-micron scale. *Biomech. Model Mechano-biol.* **2003**, *2* (1), 21–36.
- (15) Currey, J. D. Effects of differences in mineralization on the mechanical properties of bone. *Phil. Trans. R. Soc. London B* **1984**, *304*, 509–518.
- (16) Tai, K.; Qi, H. J.; Ortiz, C. Effect of mineral content on the nanoindentation properties and nanoscale deformation mechanisms of bovine tibial cortical bone. *J. Mater. Sci.-Mater. Med.* **2005**, *16*, 947–959.
- (17) Thurner, P. J.; Erickson, B.; Jungman, R.; Schriock, Z.; Weaver, J. C.; Fantner, G. E.; Schitter, G.; Morse, D. E.; Hansma, P. K. Photography of compressed human trabecular bone correlates whitening to microscopic damage. *Eng. Fracture Mech.* **2006**, (Special Issue: Mechanics of Biomaterials), doi:10.1016/j.engfracmech.2006.1005.1024.
- (18) Mitarai, N.; Nori, F. Wet granular materials. *Adv. Phys.* **2006**, *55* (1–2), 1–45.
- (19) Coulomb, C. A. *Mem. Math. Acad. R. Sci.* **1773**, *7*, 343.
- (20) Ganneau, F.; Constantinides, G.; Ulm, F.-J. Dual-indentation technique for the assessment of strength properties of cohesive-frictional materials. *Int. J. Solids Struct.* **2006**, *43* (4), 1727–1745.
- (21) Oliver, W. C.; Pharr, G. M. An improved technique for determining hardness and elastic modulus using load and displacement sensing indentation experiments. *J. Mater. Res.* **1992**, *7*, 1564–1583.
- (22) Fan, Z.; Rho, J. Y.; Swadener, J. G. Three-dimensional finite element analysis of the effects of anisotropy on bone mechanical properties measured by nanoindentation. *J. Mater. Res.* **2004**, *19* (1), 114–123.
- (23) Weinbaum, S.; Cowin, S. C.; Zeng, Y. A model for the excitation of osteocytes by mechanical loading-induced bone fluid shear stresses. *J. Biomech.* **1994**, *27* (3), 339–360.
- (24) Schofield, A. N.; Wroth, C. P. *Critical state soil mechanics*; McGraw Hill: New York, 1968.
- (25) Raviv, U.; Giasson, S.; Kampf, N.; Gohy, J. F.; Jerome, R.; Klein, J. Lubrication by charged polymers. *Nature* **2003**, *425*, 163–165.
- (26) Walsh, W. R.; Ohno, M.; Guzelsu, N. Bone composite behaviour: effects of mineral-organic bonding. *J. Mat. Sci.* **1994**, *5*, 72–79.
- (27) Eyre, D. R.; Wu, J. J. Collagen crosslinks. *Top. Curr. Chem.* **2005**, *247*, 207–229.
- (28) Knott, L.; Bailey, A. J. Collagen cross-links in mineralizing tissues: A review of their chemistry, function, and clinical relevance. *Bone* **1998**, *22* (3), 181–187.
- (29) Fantner, G. E.; Orudjev, E.; Schitter, G.; Golde, L. S.; Thurner, P.; Finch, M. M.; Turner, P.; Gutschmann, T.; Morse, D. E.; Hansma, H.; Hansma, P. K. Sacrificial bonds and hidden length: unraveling molecular mesostructures in tough materials. *Biophys. J.* **2006**, *90* (4), 1411–1418.
- (30) Ingram, R. T.; Clarke, B. L.; Fisher, L. W.; Fitzpatrick, L. A. Distribution of noncollagenous proteins in the matrix of adult human bone: evidence of anatomic and functional heterogeneity. *J. Bone Miner. Res.* **1993**, *8* (9), 1019–1029.
- (31) Braiman, Y.; Barhen, J.; Protopopescu, V. Control of friction at the nanoscale. *Phys. Rev. Lett.* **2003**, *90* (9), 094301.
- (32) Wang, R. Z.; Suo, Z.; Evans, A. G.; Yao, N.; Aksay, I. A. Deformation mechanisms in nacre. *J. Mater. Res.* **2001**, *16* (9), 2485–2493.
- (33) Hirano, M. Atomistics of friction. *Surf. Sci. Rep.* **2006**, *60*, 159–201.
- (34) Urbakh, M.; Klafter, J.; Gourdon, D.; Israelachvili, J. The nonlinear nature of friction. *Nature* **2004**, *430*, 525–528.
- (35) Wren, T. A. L.; Yerby, S. A.; Beaupre, G. S.; Carter, D. R. Influence of bone mineral density, age, and strain rate on the failure mode of human Achilles tendons. *Clin. Biomech.* **2001**, *16*, 529–534.
- (36) Aerssens, J.; Boonen, S.; Joly, J.; Dequeker, J. Variations in trabecular bone composition with anatomical site and age: potential implications for bone quality assessment. *J. Endocrinol.* **1997**, *155* (3), 411–421.
- (37) Raum, K.; Leguerney, I.; Chandelier, F.; Talmant, M.; Saied, A.; Peyrin, F.; Laugier, P. Site-matched assessment of structural and tissue properties of cortical bone using scanning acoustic microscopy and synchrotron radiation microCT. *Phys. Med. Biol.* **2006**, *51* (3), 733–746.
- (38) Morgan, E. F.; Bayraktar, H. H.; Yeh, O. C.; Majumdar, S.; Burghardt, A.; Keaveny, T. M., Contribution of inter-site variations in architecture to trabecular bone apparent yield strains. *J. Biomech.* **2004**, *37* (9), 1413–1420.
- (39) Burr, D. B.; Forwood, M. R.; Fyhrie, D. P.; Martin, R. B.; Schaffler, M. B.; Turner, C. H. Bone microdamage and skeletal fragility in osteoporotic and stress fractures. *J. Bone Miner. Res.* **1997**, *12* (1), 6–15.
- (40) Lawn, B. R.; Dabbs, T. P.; Fairbanks, C. J. Kinetics of shear-activated indentation crack initiation in soda-lime glass. *J. Mater. Sci.* **1983**, *18* (9), 2785–2797.
- (41) Fantner, G. E.; Rabinovich, O.; Schitter, G.; Thurner, P.; Kindt, J. H.; Finch, M. M.; Weaver, J. C.; Golde, L. S.; Morse, D. E.; Lipman, E. A.; Rangelow, I. W.; Hansma, P. K. Hierarchical interconnections in the nano-composite material bone: Fibrillar cross-links resist fracture on several length scales. *Comp. Sci. Technol.* **2005**, *66* (9), 1205–1211.
- (42) Landis, W. J. The strength of a calcified tissue depends in part on the molecular structure and organization of its constituent mineral crystals in their organic matrix. *Bone* **1995**, *16* (5), 533–544.
- (43) Wachtel, E.; Weiner, S. Small-angle X-ray scattering study of dispersed crystals from bone and tendon. *J. Bone Min. Res.* **1994**, *9* (10), 1651–1655.

NL061877K